

Tectonic and climatic controls on the Plio-Pleistocene evolution of sediment discharge from Papua New Guinea

Nana Peng^{a,1}, Haowen Dang^{a,*}, Jiawang Wu^{a,*}, Ivano W. Aiello^b, Zhimin Jian^a

^a State Key Laboratory of Marine Geology, Tongji University, 1239 Siping Road, Shanghai 200092, China

^b Moss Landing Marine Laboratories, 8272 Moss Landing Road, Moss Landing, CA 95039, United States

ARTICLE INFO

Keywords:

Plio-Pleistocene
Papua New Guinea
Orogenic phases
Weathering
Tropical western Pacific
IODP Site U1489

ABSTRACT

This study presents a detailed sedimentary geochemical record of International Ocean Discovery Program (IODP) Site U1489, which was drilled off the northeast margin of Papua New Guinea (PNG). Focusing on the geochemical characteristics and the extent of chemical weathering of siliciclastic component, a total of 183 samples from the upper 84 m of Site U1489 are used to reconstruct the PNG sediment supplies to the tropical western Pacific over the last 4 Ma. Our geochemical results show a 3-stage variability in Site U1489 sediment composition, which are well related to regional tectonic and climatic changes. Stages III (~4.0–3.5 Ma) and II-A (~2.9–1.7 Ma) are characterized by more enhanced and variable contributions from mafic-rock sources than that of felsic-origin. This interval is shown to be accompanied by relatively rapid sediment delivery and more dynamic depositional environments that are possibly related to marginal mixing, coinciding with more frequent PNG tectonic events. In particular, increased contributions derived from ultra-mafic/mafic rocks are recorded between ~3.5 and 2.9 Ma, which is attributed to increased ophiolite input due to arc-continent collision. Accordingly, these results give a consistent but refined timing for an accelerated plate suturing at the eastern margin of PNG. By contrast, Stage I (~1.7–0 Ma) is characterized by a relatively constant background supply of finer particles, showing a persistent increase over time in the intensity of chemical weathering. This increased weathering trend is reported for the first time for the tropical regions of western Pacific, and it is interpreted as indicating a strengthening of the Walker Circulation in the past ~1.7 Ma. Overall, the interpretations of the siliciclastic fraction from Site U1489 presented in this paper provides crucial clues to distinguish the tectonic and climatic influences on the PNG sediment inputs during the Plio-Pleistocene.

1. Introduction

Over the last ~5 million years (Ma) of the Plio-Pleistocene, Earth's climate had undergone a significant cooling, and the middle Pliocene is often taken as a future-analogous warm state (Haywood et al., 2016). The Plio-Pleistocene cooling trend is thought to be stronger in the eastern- than the western- equatorial Pacific (i.e. EEP and WEP) (Fedorov et al., 2015; Tierney et al., 2019), thus causing a gradual intensifying zonal gradient of sea surface temperature (SST) across the Pacific. This west–east SST gradient plays a decisive role in the equatorial air–sea coupled system, i.e., the El Niño Southern Oscillation (ENSO) (Philander, 1983; Wara et al., 2005). Moreover, the different oceanic and climatic conditions of the WEP in the warm Pliocene may have significantly reorganized the circulations and coupled dynamics of

the low- to middle-latitude ocean and atmosphere (Fedorov et al., 2015; Burls et al., 2017; Tierney et al., 2019). However, little is known about the Plio-Pleistocene hydrologic changes over the WEP, mainly because of the short of continuous sedimentary records (e.g. those of Yu et al., 2016, 2018 from the northern Philippine Sea yet limited to ~2 Ma).

Papua New Guinea (PNG) has the potential to provide such key lines of evidences, as it is a major island in the WEP and locates at a pivotal position in the climatic and oceanographic systems of the tropical Indo-Pacific (Fig. 1a). In the vicinity of PNG, air-flows converge to form the ascending convection center for zonal Walker and meridional Hadley Cells (Webster et al., 1998; Trenberth et al., 2000; Wang et al., 2003), and tropical sub-surface waters from both hemispheres either join into the Equatorial Undercurrent (EUC) to integrate the Pacific low-latitude shallow overturning circulation (Godfrey et al., 2001) or partly leak into

* Corresponding authors.

E-mail addresses: hwdang@tongji.edu.cn (H. Dang), jwwu@tongji.edu.cn (J. Wu).

¹ Authors who contributed equally to the work.

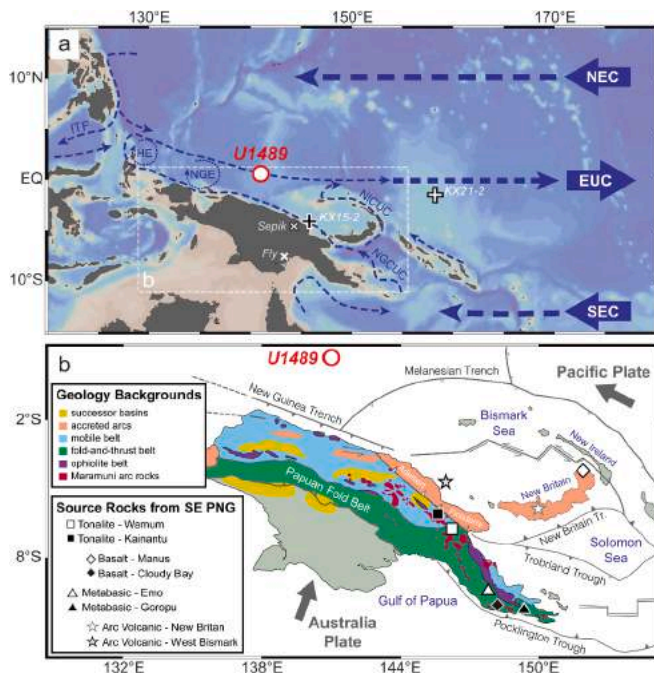


Fig. 1. Western equatorial Pacific oceanography and PNG geologic backgrounds.

(a) Schematic view of the major oceanic currents (dashed lines), including the North and South Equatorial Current (NEC, and SEC), the New Guinea and New Ireland Coastal Undercurrent (NGCUC, and NICUC), the Indonesian Throughflow (ITF), and the Equatorial Undercurrent (EUC), with two major eddies (dotted lines) of Halmahera Eddy (HE) and New Guinea Eddy (NGE) depicted (after [Fine et al., 1994](#); [Kashino et al., 2007](#)). (b) Major geological and tectonic units of the PNG region (colour annotations see Legend, after [Baldwin et al., 2012](#); [Cloos et al., 2005](#)). The locations of IODP Site U1489 (red circle), the largest rivers of PNG (i.e. Sepik and Fly, crosses), KX cores (plus-signs) and the potential source rocks from southeast PNG (symbols annotated in Legend) are marked. (For interpretation of the references to colour in this figure legend, the reader is referred to the web version of this article.)

the Indonesian Throughflow to serve as a key connect of the global thermohaline circulation ([Gordon, 2005](#)) ([Fig. 1a](#)). Changes in such hydroclimate and oceanic variations are proven to be faithfully documented in the marine sediment sequences offshore PNG during the Quaternary ([Tachikawa et al., 2011](#); [Wu et al., 2012, 2013](#); [Hollstein et al., 2018](#); [Aiello et al., 2019](#); [Dang et al., 2020a](#); and references therein), as a result of the tremendous terrigenous detrital material exported from PNG (c.f. [Milliman et al., 1999](#); [Walsh and Nittrouer, 2003](#)).

However, over the Plio-Pleistocene, the PNG region experienced drastic tectonic movements, with intensive (micro)plate convergence, arc-continent collision, sea-floor spreading, microplate rotation and magmatism (c.f. [Baldwin et al., 2012](#); [Holm et al., 2016](#)) ([Fig. 1b](#)). At timescales of million years, tectonic activities and the consequent effects of erosion/weathering are thought to play a critical role in driving the Neogene global cooling (e.g. [Molnar and England, 1990](#); [Raymo and Ruddiman, 1992](#); [Hay et al., 2002](#); [Li and Elderfield, 2011](#)). A key driving force for the Neogene cooling and glaciation, was hypothesized to be the arc-continent collision in WEP regions, which could accelerate carbon sequestration through the weathering and erosion of newly-formed mafic rocks ([MacDonald et al., 2019](#)). Although, many key aspects about the weathering processes are still under debate, especially the lithologic effect of uplifted landmass on weathering intensity and carbon consumption flux (e.g. [Gaillardet et al., 1999](#); [Caves Rugenstein et al., 2019](#); [Lu et al., 2020](#)). In the context of the chemical weatherability, the Southeast Asian areas with newly exhumed mafic/ultramafic rock, like those Late Cenozoic terranes of PNG, have the highest

chemical weathering flux and contribute a prominent proportion of the global CO₂ consumption due to weathering ([Hartmann et al., 2009](#); [Hartmann et al., 2014](#)).

Previous studies have shown that, changes in the tectonic configurations of the PNG and WEP regions have profound consequences on not only the regional oceanic (e.g. Pacific-Indian linkage) and climatic states (e.g. Australia aridification, [Christensen et al., 2017](#)), but also the biogeochemical cycling along the equatorial Pacific ([Wells et al., 1999](#)). Most importantly, for the evolution of the Equatorial Pacific W-E thermal contrast in the last ~8 Ma, the gradual closure of the Panama Seaway was proposed as a major control ([Keller et al., 1989](#); [Zhang et al., 2012](#)). As a result, besides climate change, a thorough understanding of the basement rocks, sedimentation dynamic and weathering products, in association with regional tectonics, is necessary for comprehensive interpretations of the marine sedimentary records.

Therefore, to investigate changes in tectonic activities and related sediment transport of the PNG region, which are fundamental for the regional configuration of paleoceanography and paleoclimate, this study analyzed samples from the International Ocean Discovery Program (IODP) Site U1489 ([Fig. 1](#)), one of the series of off-PNG sites drilled by the IODP Expedition 363. A total of 183 samples are selected from the upper ~84 m of Site U1489 ([Rosenthal et al., 2018](#)), processed for siliciclastic component, and analyzed for major and trace elements including rare earth elements (REE). We provide, for the first time, a continuous sedimentary record covering the last 4 Ma to fill an important gap on our understanding of the regional hydroclimatic and oceanic changes that occurred offshore PNG. The elemental geochemical data allow us to separate between the effects of changes in siliciclastic input due to tectonism from climate-driven variations in weathering intensity over the last 4 Ma. The deconvolution of the overlapping effects of different factors such as sediment provenance, transport dynamics, and weathering intensity, significantly improves our understanding of the major phases of PNG orogenesis, as well as for the shifts of climate-state over the equatorial Pacific.

2. Background settings

2.1. PNG geology

The PNG region straddles an active island-arc junction primarily between the converging Australian and Pacific Ocean Plates ([Fig. 1](#)), and thus has various kinds of geodynamic processes taking place mainly in the Late Neogene ([Baldwin et al., 2012](#); [Holm et al., 2016](#)). The northwest-to-southeast extending Central Range, which intensively uplifted during the late Miocene and early Pliocene ([Hill and Raza, 1999](#)), divides the PNG Island to a southwestern half with the Australian continental crust underlain and a northeastern half with Melanesian Arc Terranes built upon Mesozoic oceanic crust ([Cloos et al., 2005](#); [Baldwin et al., 2012](#)). From the continent to the ocean, the PNG region consists of five major litho-tectonic units: (1) a foreland basin, (2) a highland fold-and-thrust belt, (3) an underlying metamorphic belt, (4) an upturned forearc basement (with overlying ophiolite complex), and (5) an accreted oceanic arc complex ([Fig. 1b](#), [Davies and Jaques, 1984](#); [Cloos et al., 2005](#)). Due to active plate/microplate collisions, mafic volcanic and other metamorphic rocks are well developed in the PNG region. In the northern PNG, the Irian Ophiolite Belt of Jurassic age overlying the Ruffaer metamorphic belt, is upturned and sutured to form the north flank of the Central Range since the late Miocene ([Fig. 1b](#), [Cloos et al., 2005](#)). In the eastern PNG, the Adelbert-Finisterre-New Britain collision during the middle Pliocene, resulted in widespread accretion of ophiolite and ultramafic rocks ([Fig. 1b](#), [Abbott et al., 1994](#); [Abbott, 1995](#)).

2.2. WEP oceanography

The WEP is a water-mass crossroad where the low-latitude western boundary currents from both North and South Pacific converge into the

equatorial undercurrents (Fig. 1a, Fine et al., 1994). The North and South Pacific Equatorial Currents (NEC and SEC, respectively) transport sub-surface and intermediate waters from the subtropics into the equatorward western boundary currents, which retroflect via several local eddies into the eastward flowing currents represented by the Equatorial Undercurrent (EUC) (Fig. 1a, Fine et al., 1994). The Indonesian Throughflow (ITF), on the other hand, leaks the Pacific waters into the Indian Ocean (Gordon, 2005). Currents offshore the PNG region includes: (1) monsoon-driven seasonally reversed New Guinea Coastal Current (NGCC), (2) the equatorward flowing New Guinea Coastal Undercurrent (NGCUC) and (3) the equatorward flowing New Ireland Coastal Undercurrent (NICUC), which serve as the major pathways of SEC converging into the Equatorial Pacific (Fig. 1a). The NGCUC originates from the SEC around the Great Barrier Reef, and finally flows along the PNG coast after circulating in the Gulf of Papua (Tsuchiya et al., 1989; Grenier et al., 2011). The NICUC, originating too from SEC but flowing eastern off the New Ireland, ultimately joins half its volume into the NGCUC in the Bismarck Sea and retroflects the other half directly into the EUC (Fig. 1a, Butt and Lindstrom, 1994; Melet et al., 2010). The contribution of NGCUC is estimated to be up to 62% of the EUC at 145°E, and about 50% at 156°E after NICUC has joined in (Slemons et al., 2010). As a result, the NGCUC and NICUC are powerful in delivering the terrigenous matters from the PNG region to the WEP.

2.3. WEP climate

The WEP area experiences the Earth's most expansive and persistent low-level moisture convergence, given the existence and variations of the Inter-tropical Convergence Zone (ITCZ), the South Pacific Convergence Zone (SPCZ) and the ascending limb of the Walker Cell (WC) (Vincent, 1994; Webster et al., 1998; Yim et al., 2016). The meridional displacement of ITCZ over WEP tightly follows the Australasian monsoon and brings slightly more rainfall to the PNG region during austral summer on a seasonal base (Webster et al., 1998). A strong atmospheric link over the PNG and the southwestern subtropical Pacific generates circulation anomalies of the SPCZ (merges with ITCZ over PNG), which further converges the South Pacific northeasterly trade winds and the southeasterlies from Australia, and resulted in abundant rainfall year-round over the PNG region (Kiladis et al., 1989; Vincent, 1994). On the modern inter-annual scale, the shift between El Niño and La Niña events modulates the strength and location of the ascending limb of WC, presumably causing reduced rainfall over PNG during El Niño phases (Yim et al., 2016). On the other hand, shifts of SPCZ in association with ENSO generate more severe consequences to the rainfall over the WEP. During extreme El Niño events, essentially due to a substantial reduction in zonal and meridional SST gradients, the SPCZ shifts equatorward and severe droughts occur over the WEP islands (Cai et al., 2012; Borlace et al., 2014).

3. Materials and methods

3.1. Site U1489 and its chronology

Sediment cores at Site U1489 (02°07.19'N, 141°01.67'E, 3421 m water depth) were drilled during IODP Expedition 363 near the bottom of the western flank of the southern Eauripik Rise, Caroline Sea (Fig. 1). Drilling at Site U1489 penetrated a continuous succession of hemipelagic, carbonate-rich sediment, and the recovered sequences mainly consist of nannofossil ooze and chalk with varying proportions of clay minerals (Rosenthal et al., 2018). For this study, 2-cm-thick half-round samples were collected at a ~ 50-cm interval along the splice (a complete sedimentary sequence of the site, based on patching together the sequences recovered from different holes) from the upper 84 m of Site U1489, resulting in 183 samples in total. A first $\delta^{18}\text{O}$ -stratigraphic age model for the upper ~84 m sediment succession of Site U1489 was established by benthic foraminifera $\delta^{18}\text{O}$ analysis on the same samples

as shown in this study (Dang et al., 2020b). Due to the relatively low time-resolution of the sampling strategy, only some major Marine Isotope Stages were recognized in the last ~2.9 Ma, beyond which the age model relies on the paleo-magnetic reversals defined by ship-board studies (Dang et al., 2020b). Based on the estimated sedimentation rates ranging between 1.2 and 3.4 cm/ka, the samples of this study yield a mean time-resolution of ~15–42 ka (Dang et al., 2020b). Given an average uncertainty of <10 ka of the age determinations, variations on a timescale longer than 100 ka (i.e. >0.1 Ma) are considered statistically significant.

3.2. Siliciclastic sediment geochemistry

Detrital, aluminosilicate fraction was isolated by removing all potential biogenic fractions. Noting that some samples in Site U1489 have considerable opal contents (Rosenthal et al., 2018), for each sample, about 200 mg bulk sediments were leached by (1) hydrogen dioxide (10% in volume) to remove organic material, (2) sodium hydroxide solution (1 M) to remove possible biogenic silicon, and (3) hydrochloric acid solution (0.05 M) to remove calcium carbonate. Subsequently, the detritus residues were centrifuged and oven-dried at 55 °C for over 24 h, and then ground in an agate mortar into fine powder.

Approximately 50 mg powdered residues were digested with a mixture solution of concentrated HNO_3 and HF on a hot plate, and the eluted samples were diluted by 2% HNO_3 for geochemical measurements (c.f. Li et al., 2003; Wei et al., 2003; Shao et al., 2017). Major, trace and rare earth elements were determined by an Inductively Coupled Plasma-Optical Emission (ICP-OES, Thermo ICP-IRIS Intrepid II) and an Inductively Coupled Plasma-Mass Spectrometry (ICP-MS, Thermo X-Series), respectively. Each sample was measured up to 6 times with 1 ppb of Ru as an internal standard, as detailed in Li et al. (2002). Analytical precision and accuracy were monitored by replicate analyses of international certified materials (GSR-5, GSR-6, and GSD-9), suggesting that the relative deviations are mostly less than 6%. All the pretreatments, measurements and analyses were performed at the State Key Laboratory of Marine Geology, Tongji University.

3.3. Indexes of chemical weathering

Three different indexes of chemical weathering are used, including the Chemical Index of Alteration (CIA; Nesbitt and Young, 1982), Chemical Index of Alteration that excludes CaO (CIX; Garzanti et al., 2014) and the Index of Compositional Variability (ICV; Cox et al., 1995). The CIA and CIX are calculated using molecular proportions of mobile and alkaline-earth metals, with higher values suggesting stronger weathering and vice versa (Table 1). No correction for biogenic Ca was applied because our results are on a carbonate-free basis. As the most widely used weathering index, the CIA (and CIX) indicate the extent of conversion of feldspars to clay minerals like the kaolinite that is enriched in Al (Liu et al., 2012; Garzanti et al., 2014). It is suggested that the CIA essentially reflect the integrated weathering history rather than

Table 1
Calculation of the weathering indexes used.

Index ^a	Formula ^b
CIA ^c	$= \text{Al}_2\text{O}_3 / (\text{Al}_2\text{O}_3 + \text{K}_2\text{O} + \text{CaO}^* + \text{Na}_2\text{O}) \times 100$
CIX	$= \text{Al}_2\text{O}_3 / (\text{Al}_2\text{O}_3 + \text{K}_2\text{O} + \text{Na}_2\text{O}) \times 100$
ICV ^{c,d}	$= (\text{CaO}^* + \text{K}_2\text{O} + \text{Na}_2\text{O} + \text{Fe}_2\text{O}_3^{\#} + \text{MgO} + \text{MnO} + \text{TiO}_2) / \text{Al}_2\text{O}_3$

^a CIA: Chemical Index of Alteration (Nesbitt and Young, 1982); CIX: CIA that excludes CaO (Garzanti et al., 2014); ICV: Index of Compositional Variability (Cox et al., 1995).

^b Units for CIA and CIX are in molar proportions, while for ICV is in mass weight.

^c CaO* refers to the calcium oxides exclusive of carbonates.

^d Fe₂O₃[#] refers to the total iron oxides.

the instantaneous intensity of chemical weathering in continents (Li and Yang, 2012).

Neither of the CIA and CIX indexes is sensitive to the lithology of parent rocks. On the other hand, the ICV is calculated by mass fractions of major elements including Fe, Mg, Mn, and Ti (Table 1); and tend to be highest during the weathering of pyroxene and amphibole and decrease with the weathering of more stable minerals like alkali-feldspars (Cox et al., 1995). Therefore, by incorporating heterogeneous sources including metamorphic rocks, the ICV evaluates the compositional maturity of the sediments by taking the parent-rock types into account, making it a more appropriate weathering index for mafic source terrains (Lee, 2002; Price and Velbel, 2003; Borges and Huh, 2007).

4. Results

4.1. Major/minor elements and weathering indexes

To assess the elemental composition and to discount the potential dilution effects, major and minor elements (e.g. Na, Ca, K, Ti) are reported with respect to Al, as well as the ratios of K/Rb and Zr/Rb (Fig. 2). There is a striking similarity between the profiles of Na/Al and Ca/Al, showing a slight increase from ~4.0 to 2.9 Ma, followed by a continuous decrease from ~2.3 Ma till the present (Fig. 2a).

Notably, there is a close correspondence between the ratios of Ti/Al and Zr/Rb, showing generally enhanced values before than after ~1.7 Ma, with highest values between ~2.9 and 1.7 Ma (Fig. 2b, c). The correspondence between the refractory elements (i.e. Zr and Ti) indicates the same first-order control on their secular variations, which must be different from the controlling factor on the much more soluble elements (i.e. Na and Ca) although the changing patterns are quite similar (Fig. 2a, c).

In between, K/Al profile is characterized by a gradual increase over the last ~1.3 Ma (Fig. 2b), displaying a reverse pattern to the decreasing Na/Al and Ca/Al in this interval (Fig. 2a). Moreover, K/Rb ratio exhibit similar yet more spiked variations compared to those of Ti/Al and Zr/Rb (Fig. 2b, c).

Regardless of the different calculations (Table 1; also see Section 3.3), the various indexes of weathering such as CIA, CIX, and ICV exhibit a nearly identical variability (Fig. 2d–f), which generally mirrors those of Na/Al and Ca/Al ratios (Fig. 2a). Although the consistent variations as shown by different indexes confirm the changing trends of weathering intensity (Fig. 2d–f), the absolute CIA values are relatively low (i.e. between 40 and 70), indicating that processes other than weathering and erosion play a role (see Section 5).

4.2. Trace elements including rare earth elements (REE)

With normalization to the upper continental crust (UCC; Rudnick and Gao, 2003), the trace-element distribution of Site U1489 sediments exhibit a clear pattern between mafic and felsic elements (Figs. 3 and 4). The pattern is relatively invariable, showing prominent enrichments in the transition elements of Sc, V, Cr, Ni, and somewhat Co that are typically enriched in mafic igneous rocks, and depletions in the elements of Rb, Y, Zr, Nb, and Th that are more concentrated in felsic rocks (c.f. McLennan et al., 1993) (Fig. 4). Ratios of Ni/Th and Cr/Rb are taken to indicate the relative contributions between mafic and felsic origins (Fig. 3d). The profiles of Ni/Th and Cr/Rb are highly similar, showing enhanced values between ~4.0 and 2.9 Ma, and lowered values from ~2.9 to 1.7 Ma. After a sudden rise at ~1.7 Ma, the ratios gradually decrease (Fig. 3d).

When normalized to the UCC (Rudnick and Gao, 2003), the REE fractionation pattern of Site U1489 sediments show relatively narrow variations, which are characterized by positive Eu anomalies and depletion of light REE (LREE: La to Nd) relative to the middle (M) and heavy (H) REE (MREE: Sm to Gd; HREE: Dy to Lu) (Figs. 3 and 5). Based on these characteristics, useful parameters of REE fractionation are

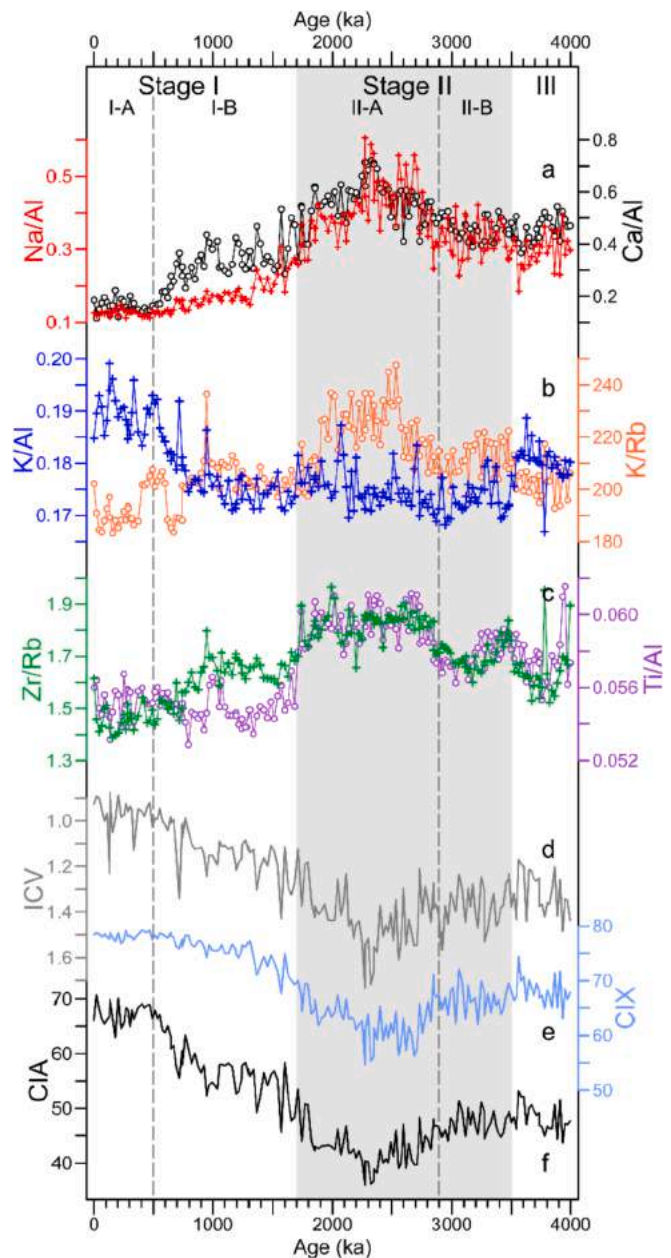


Fig. 2. Major-element composition of siliciclastic sediments of IODP Site U1489.

(a) Elemental ratios of Na/Al (red with plus-signs) and Ca/Al (black with circles). (b) K/Al (blue with plus-sign) and K/Rb (orange with circles). (c) Proxies of sediment grain size: Zr/Rb (green with plus-signs; e.g. Schneider et al., 1997) and Ti/Al (purple with circles; e.g. Boyle, 1983). (d–f) Indexes of weathering intensity: ICV (d, gray; Cox et al., 1995), CIX (e, gray blue; Garzanti et al., 2014) and CIA (f, gray; Nesbitt and Young, 1982). The unit for elemental ratio is g/g. Stage I (1.7–0 Ma) with sub-stages I-A (0.5–0 Ma) and I-B (1.7–0.5 Ma), Stage II (3.5–1.7 Ma) with sub-stages II-A (2.9–1.7 Ma) and II-B (3.5–2.9 Ma), and Stage III (4.0–3.5 Ma) are shown by vertical bars and dashed lines (see Section 4.3). (For interpretation of the references to colour in this figure legend, the reader is referred to the web version of this article.)

extracted, all of which show consistent downcore variations (Fig. 3).

The total, UCC-normalized REE concentrations (i.e. Σ REE, and so on) exhibit a stepwise pattern; after a generally decreasing trend from ~4.0 to 2.3 Ma, the Σ REE persistently increases till today (Fig. 3a). Mirror wise, the Eu anomaly (i.e. Eu/Eu^* , as calculated by $\text{Eu}_N/(\text{Sm}_N \times \text{Gd}_N)^{1/2}$) has large-amplitude variations from ~4.0 to 2.9 Ma, followed by a persistent decrease (Fig. 3a). For the relative enrichment/depletion of

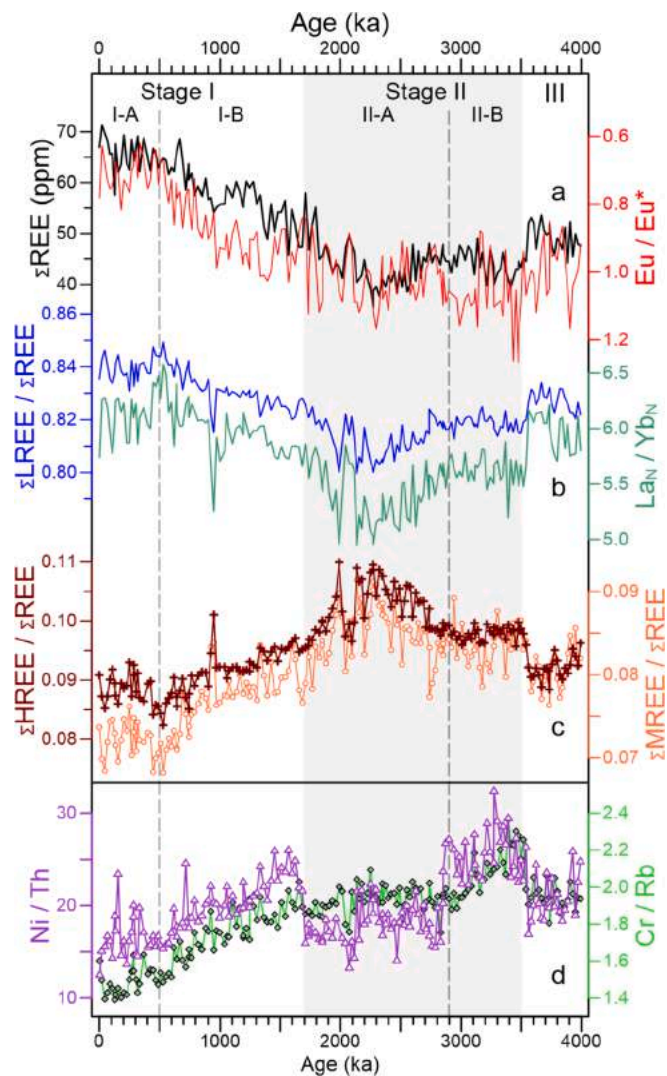


Fig. 3. Trace-element composition of the siliciclastic sediments of IODP Site U1489.

(a) Total REE concentration (ΣREE , black), and the Eu anomaly ($\text{Eu}/\text{Eu}^* = \text{Eu}_N/(\text{Sm}_N \times \text{Gd}_N)^{1/2}$, red). (b) Ratio of light REE to heavy REE ($\Sigma\text{LREE}/\Sigma\text{REE}$, blue), which is often approximated by La versus Yb (La_N/Yb_N , the subscript N refers to chondrite-normalized, green). (c) Ratios of heavy REE ($\Sigma\text{HREE}/\Sigma\text{REE}$, brown with plus-signs) and middle REE ($\Sigma\text{MREE}/\Sigma\text{REE}$, orange with circles) to total REE, respectively. Note that all REE data are normalized to chondrite (McDonough and Sun, 1995). (d) Selected elemental ratios indicative of the mafic versus felsic contributions (c.f. McLennan et al., 1993): Ni/Th (purple with triangles) and Cr/Rb (light green with diamonds). Stage I (1.7–0 Ma) with sub-stages I-A (0.5–0 Ma) and I-B (1.7–0.5 Ma), Stage II (3.5–1.7 Ma) with sub-stages II-A (2.9–1.7 Ma) and II-B (3.5–2.9 Ma), and Stage III (4.0–3.5 Ma) are shown by vertical bars and dashed lines (see Section 4.3). (For interpretation of the references to colour in this figure legend, the reader is referred to the web version of this article.)

LREE, various ratios of $\Sigma\text{LREE}/\Sigma\text{REE}$, $\Sigma\text{MREE}/\Sigma\text{REE}$, $\Sigma\text{HREE}/\Sigma\text{REE}$, and La_N/Yb_N clearly show a three-stage variability (Fig. 3b, c; see Section 4.3). Notably, the LREE/HREE is often approximated by the ratio of La_N/Yb_N . Also note that the subscripts N refers to chondrite normalization (McDonough and Sun, 1995), while subscript C refers to UCC-normalized (Rudnick and Gao, 2003).

4.3. Three stages defined by compositional changes

Taken together, the temporal variations in the geochemical compositions of Site U1489 sediments can be consistently divided into three

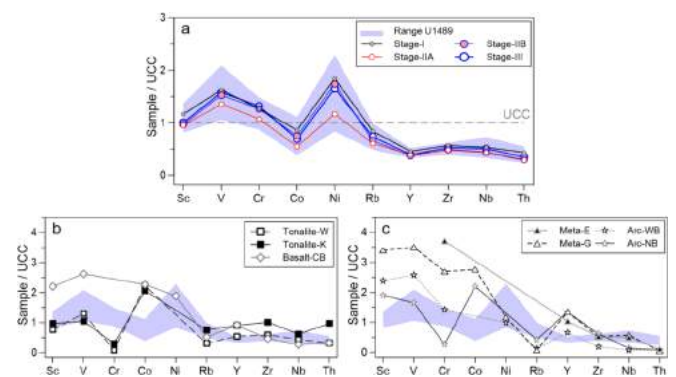


Fig. 4. Trace-element distribution pattern of IODP Site U1489 sediments. (a) Sediment samples of Site U1489, showing the distribution range of all samples (light blue shading; also in b–c) and the average values for the evolutionary stages (lines with symbols). (b) Tonalites (squares; Holm et al., 2015) from Wamum (Tonalite-W) and Kainantu (Tonalite-K), and basalts (diamonds) from the Cloudy Bay (Basalt-CB; Holm and Poke, 2018). (c) Metamorphic rocks (triangles) from Emo (Meta-E; Zirakparvar et al., 2013) and Goropu (Meta-G; Smith, 2013), and arc volcanic rocks (stars) from New Britain (Arc-NB; Holm et al., 2013) and Western Bismarck arc (Arc-WB; Woodhead et al., 2010). Note that the transition elements Sc, V, Co, Cr, and Ni are typically enriched in mafic igneous rocks, whereas Rb, Y, Zr, Nb, and Th are more concentrated in felsic rocks (c.f. McLennan et al., 1993). All trace elements are normalized to mean values of the upper continental crust (UCC; Rudnick and Gao, 2003). See Fig. 1b for the locations of the potential source rocks. (For interpretation of the references to colour in this figure legend, the reader is referred to the web version of this article.)

stages (Figs. 2 and 3), from top to bottom:

- Stage I: from ~1.7 to 0 Ma, with sub-stages I-A (~0.5–0 Ma) and I-B (~1.7–0.5 Ma);
- Stage II: from ~3.5 to 1.7 Ma, with sub-stages II-A (~2.9–1.7 Ma) and II-B (~3.5–2.9 Ma);
- Stage III: from ~4.0 to 3.5 Ma.

Specifically, such a division of the major stages relies mostly on the distinct features of Stage II, characterized by 1) increased ratios of Na/Al, Ca/Al, K/Al, K/Rb, Ti/Al, and Zr/Rb (Fig. 2), and 2) increased Eu/Eu* values and relatively decreased LREE contents as approximated by La_N/Yb_N (Fig. 3). Besides, Stages I and II are further divided into two sub-stages (i.e. -A and -B), respectively, not only according to the compositional variations in our geochemical results, but also consistent with the regional tectonic and climatic configurations inferred from literature, as discussed below.

5. Discussion

Geochemical composition of marine sediments has a great potential to provide information on sediment provenance, weathering intensity, and transport dynamics. Lithology in provenance areas – mafic versus felsic parent rocks – is the primary source of compositional difference (McLennan et al., 1993; Fralick and Kronberg, 1997). For instance, unweathered felsic rocks (e.g. granites) have higher Al-normalized concentrations of Rb, Y, Zr, Nb, and Th than unweathered mafic rocks (e.g. basalts) (Price and Velbel, 2003; Yang et al., 2008; Wu et al., 2013), because all these elements are relatively incompatible in mantle rocks and thus become concentrated in the crust (McDonough and Sun, 1995; Rudnick and Gao, 2003).

Chemical weathering can exert a significant influence (c.f. Gaillardet et al., 1999). Specifically, areas of intense weathering generate mature sediments characterized by strong cation depletion (e.g. Na^+ , Ca^{2+} , Mg^{2+} , and K^+) and concentration of resistant elements (e.g. Al, Ti, Zr, and Th), whereas limited weathering yields immature sediments that are compositionally similar to their parent rocks (Nesbitt and Young, 1982; Vital and Statterger, 2000; Oliva et al., 2003; Liu et al., 2012). However,

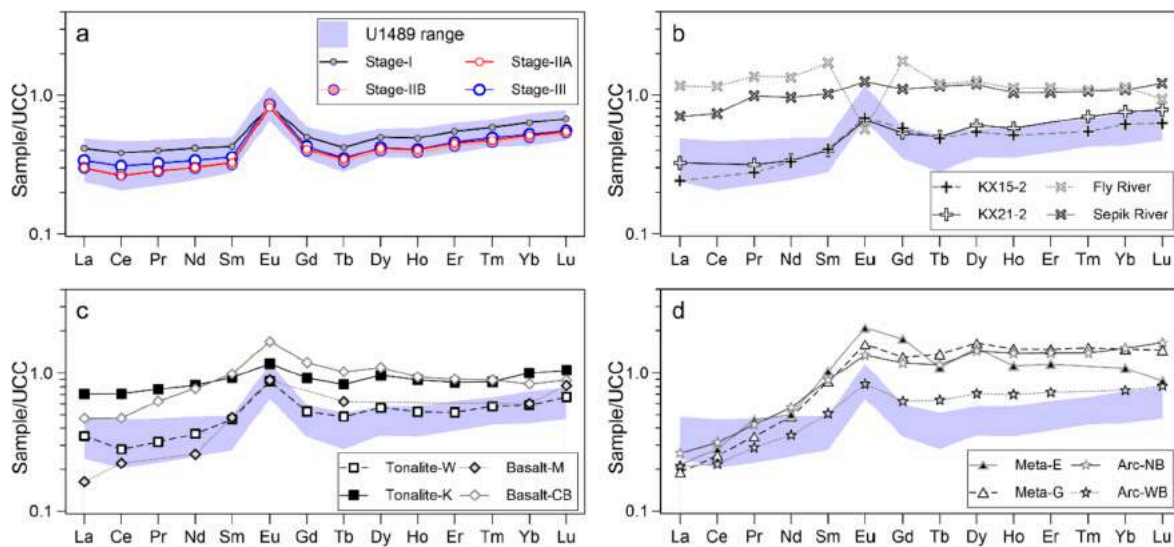


Fig. 5. REE fractionation patterns of IODP Site U1489 sediments in comparison with modern PNG-sourced sediments and potential source rocks. (a) Sediment samples of Site U1489, showing the distribution range of all samples (light blue shading; also in b–d) and the average values for the evolutionary stages (lines with symbols). (b) Modern sediments from two major PNG rivers (crosses; (Hannigan and Sholkovitz, 2001) and from the KX-cores off northern PNG (plus-signs; Wu et al., 2013). (c) Tonalites (squares; Holm et al., 2015) from Wamum (Tonalite-W) and Kainantu (Tonalite-K), and basalts (diamonds) from Manus Islands (Basalt-M; Gena et al., 2001) and the Cloudy Bay (Basalt-CB; Holm and Poke, 2018). (d) Metamorphic rocks (triangles) from Emo (Meta-E; Zirakparvar et al., 2013) and Goropu (Meta-G; Smith, 2013), and arc volcanic rocks (stars) from New Britain (Arc-NB; Holm et al., 2013) and Western Bismarck arc (Arc-WB; Woodhead et al., 2010). All REE data are normalized to mean values of the upper continental crust (UCC; Rudnick and Gao, 2003). See Fig. 1 for the locations of the rivers, KX-cores, and potential source rocks. (For interpretation of the references to colour in this figure legend, the reader is referred to the web version of this article.)

continental weathering is strongly modulated by tectonic movement and climatic conditions (Raymo and Ruddiman, 1992; West et al., 2005; Li and Elderfield, 2011; MacDonald et al., 2019). Tectonic uplift enhances the rates of physical weathering relative to chemical weathering, and contributes to the compositional and mineralogical immaturity of marine sediments via rapid erosion and deposition (Milliman et al., 1999; Walsh and Nittrouer, 2003; Wei and Algeo, 2020).

Changes in the Plio-Pleistocene sediment sequence of Site U1489, as seen from the geochemical results, must be influenced by multiple factors of weathering, tectonism, and associated transportation. As generalized above, such complex processes make it necessary, firstly, to discuss and motivate the use of various geochemical proxies (Section 5.1.1), and to determine the provenance pattern for Site U1489 sediments (Section 5.1.2). Subsequently, the inferred compositional changes in Site U1489 sediments are characterized by a stage-wise pattern (Section 5.2.1), which is tightly related to the major tectonic events that shaped the present PNG (Section 5.2.2). Finally, by deconvolving the influence of tectonism, our results suggest persistently increasing weathering intensity since the Middle Pleistocene over the western tropical Pacific, possibly linked to the strengthening trend of the Walker Cell in the Pleistocene (Section 5.3).

5.1. Geochemical proxies and sediment provenance

5.1.1. Application of geochemical proxies

Variations in the intensity of chemical weathering should result in divergent trends among the detrital elements, related to the varying degrees of elemental mobility. For Site U1489, the observation that the profiles of Na/Al and Ca/Al are similar but different from – sometimes exactly reverse to (i.e. since ~1.5 Ma) – that of K/Al, suggests that the chemical weathering is merely moderate and not sufficiently intense to leach K (Fig. 2a, b). In other words, the weathering should have depleted the elements more soluble than K (e.g. Na, Ca, Mg), while concurrently enriched the elements less or equally soluble than K (e.g. K, Al, Ti, Zr, Th) (Middelburg et al., 1988; Rubin et al., 1993). The moderately intense weathering and the consistent trends are also indicated by the various indexes of CIA, CIX, and ICV, showing a persistent increase in

weathering intensity since at least ~1.7 Ma (Fig. 2d–f). In our case, therefore, the ratios of Ca/Al and K/Al as well as the ICV indexes are chosen to reflect the weathering processes, as ICV serves better as an index for weathering of (ultra-)mafic source terrains than CIA or CIX (see Methods 3.3).

For the highly refractory and insoluble elements, the tight correspondence between K/Rb, Zr/Rb, and Ti/Al ratios points to a different first-order control on their secular changes rather than weathering (Fig. 2b, c). The similarity between Ti/Al and Zr/Rb profiles excludes the major role of sediment provenance changes, as Ti and Zr are respectively enriched in mafic and felsic rocks (Fig. 2c). Instead, these consistent changes can best be attributed to sediment grain size, in response to the varying ratios between silt and clay fractions. The motivation is as follows. Firstly, the silt fraction tends to retain the relatively mobile element K (e.g. K-feldspar) than highly weathered clays (Lange et al., 1966). Instead of forming discrete mineral phases, Rb substitutes readily for K in aluminosilicate minerals, and the enrichment of Rb relative to K is greater in mica compared to the co-existing feldspars (Lange et al., 1966; Dypvik and Harris, 2001). Secondly, much larger amounts of resistant elements like Ti and Zr are concentrated in the silt than clay fractions, as they are typically presented in heavy, refractory minerals (e.g. rutile and anatase for Ti; zircon and sphene for Zr) (Boyle, 1983; Schneider et al., 1997; Taboada et al., 2006). These features have made K/Rb, Zr/Rb, and Ti/Al as widely used grain-size proxy (e.g. Matthewson et al., 1995; Kroon et al., 2000; Dypvik and Harris, 2001; Liu et al., 2004; Sun et al., 2008).

Moreover, this inference is supported by several lines of evidence. First, the strong correlations between Al, Ti, and Zr concentrations indicate a single dominant provenance, thereby precluding the possibility of change in sediment provenance and mixing (see the plots and data in Supplementary File). Second, the similar trends as observed for the ratios normalized to Al between the highly soluble elements (i.e. Na/Al, Ca/Al) and the highly insoluble elements (i.e. Ti/Al, Zr/Al) suggest process other than chemical weathering playing a role (Fig. 2a–c). Third, the use of Zr/Rb and Ti/Al ratios as grain-size proxy is corroborated by their correspondence with the changes in total REE concentrations (Figs. 2 and 3).

Although the REE concentrations may be affected by intense chemical weathering and diagenesis (Nesbitt and Markovics, 1997; Bayon et al., 2020), most studies suggest that sediment provenance play a dominant role in determining REE composition (Condie, 1991; Yang et al., 2002; Wu et al., 2013, 2018; Pham et al., 2019). Here, the REE fractionation pattern and associated parameters (e.g. Eu/Eu^* , La_N/Yb_N) as well as the mafic/felsic element ratios (i.e. Ni/Th and Cr/Rb) are used as tracers of parent rocks and potential sources.

In the following, applications of the geochemical proxies, as motivated above, allow us to explore how these factors including sediment provenance, transport dynamics, and weathering intensity interacted with each other and dominated in the different time intervals.

5.1.2. Provenance of U1489 sediments

Characterized by positive Eu anomaly and relative LREE depletion, the UCC-normalized REE fractionation pattern of U1489 sediments is similar to those of various sediments sourced from PNG, including the particles in northern PNG rivers (e.g. Sepik River), and the marine sediments collected along the northern PNG margin (e.g. core KX15–2) and from the western equatorial Pacific (e.g. core KX21–2) (Fig. 5a, b; also see Fig. 1a for locations). This is consistent with previous studies on the late-Quaternary sediments (Wu et al., 2012, 2013; Dang et al., 2020a; and references therein), suggesting that the northern PNG riverine inputs are the main source of the siliciclastic sediments in the region and that sediment transport is largely controlled by offshore coastal currents (Fig. 1a; also see Section 2).

This interpretation may hold true only for the last ~0.5 Ma, and little is known about the terrigenous inputs from PNG in the geological past with active tectonic events. The comparison of the results from Site U1489 with the REE signatures of rocks that were exposed, dredged, or drilled in the ocean region surrounding PNG can offer further clues (Fig. 5a, c, d; also see Fig. 1b for locations). The comparison shows that, the REE signature of Site U1489 sediments is highly similar to those of the igneous rock outcrops, including the basalts from Manus Islands (i.e. Basalt-M; Gena et al., 2001) and from the Cloudy Bay (i.e. Basalt-CB; Holm and Poke, 2018), and the Tonalites from Wamum and Kainantu (i.e. Tonalite-W and -K, respectively; Holm et al., 2015) (Fig. 5c). By contrast, the overall range of U1489 sediments show a less prominent LREE depletion than those of metamorphic rocks from the southeastern PNG (including Emo, i.e. Meta-E; Zirakparvar et al., 2013; Goropu, i.e. Meta-G; Smith, 2013), and the arc volcanic rocks from New Britain (i.e. Arc-NB; Holm et al., 2013) and from Western Bismarck arc (i.e. Arc-WB; Woodhead et al., 2010). (Fig. 5d).

By and large, we propose that the major source of U1489 sediments is the mafic igneous rocks from the north and east of PNG. Moreover, although the potential input from arc volcanic rocks and metamorphic rocks may be secondary in quantity, it is characterized by a stronger LREE depletion (Fig. 5), and its contribution changes are tightly associated with the different phases of tectonic activity in PNG. In fact, variations in the relative contributions from these sources should have determined the subtle differences between the evolutionary stages and sub-stages recognized at Site U1489 (Fig. 4).

This inference is supported by the trace-element composition. In terms of UCC-normalized trace-element distribution, the siliciclastic sediments of Site U1489 show a consistent pattern, with enrichments of the elements typically concentrated in mafic rocks (e.g. Sc, V, Cr, Ni) and depletions of the elements that are more enriched in felsic rocks (e.g. Th, Nb, Zr, Y, Rb) (McLennan et al., 1993; Yang et al., 2008; Wu et al., 2013; Dang et al., 2015) (Fig. 4). This clearly indicates the predominance of ultra-mafic/mafic source rocks, along with minor felsic-rock source (Fig. 4). Moreover, the felsic contribution appears to be compositionally constant over the last 4 Ma, as indicated by the narrow ranges of variations in Th, Nb, Zr, Y, and Rb (Fig. 4) and by the linear correlation of Th_C vs. Rb_C (note that the subscript C refers to UCC-normalized; Rudnick and Gao, 2003) (Fig. 6d). On the contrary, the much larger compositional variations in the typically mafic-origin elements (Fig. 4) suggest a

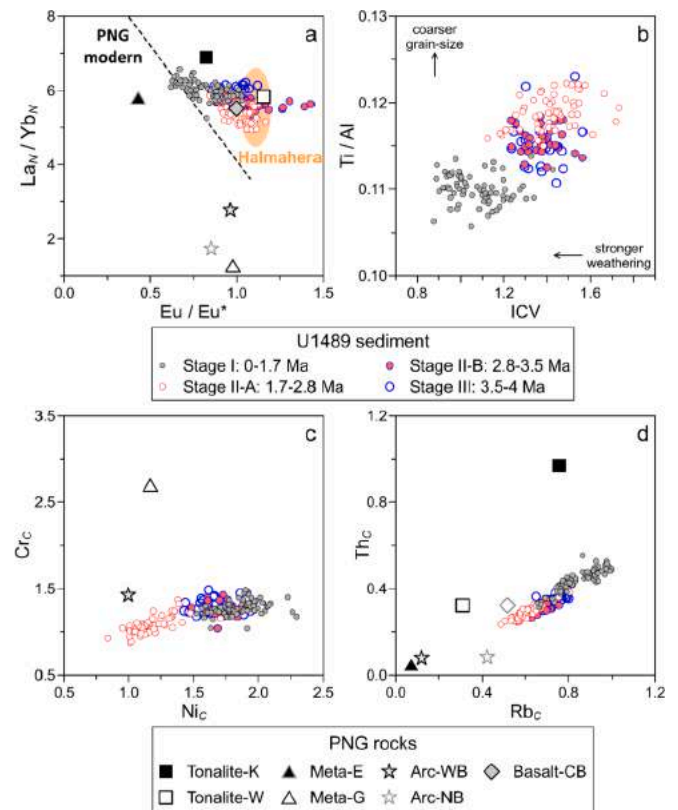


Fig. 6. Plots of extracted proxies for provenance determination of IODP Site U1489 sediments.

(a) La_N/Yb_N vs. Eu/Eu^* (McDonough and Sun, 1995). Gray dashed line shows the regression line as defined by the modern PNG-derived sediments (Wu et al., 2013) and the yellow ellipse shows the range of the Halmahera-Sea sediments (Dang et al., 2015). (b) Ti/Al vs. ICV , distinguishing the influences between transport process (by the grain-size proxy of Ti/Al) and weathering intensity (as proxied by ICV ; also see Fig. 2). (c, d) Plots of Cr_C vs. Ni_C and of Th_C vs. Rb_C (the subscript C refers to UCC-normalized; Rudnick and Gao, 2003), respectively, showing possible compositional changes in the mafic and felsic contributions. The data of Site U1489 are distinguished between the three stages, and the reference data – if available – are also plotted (annotated in Legend). See Fig. 1b for the locations of the potential source rocks. (For interpretation of the references to colour in this figure legend, the reader is referred to the web version of this article.)

complex pattern of the mafic-rock sourced contributions, which must have considerably changed across the stages (Fig. 6c). Although the reference data available so far as plotted in Fig. 4 does not allow us to distinguish the influences between ultra-mafic and mafic rocks, the additions of arc-volcanic and metamorphic rocks is supported by largest compositional variations in Ni, V, and Co that are most enriched in the ultra-mafic minerals such as olivine and spinel (Fig. 4).

5.2. Relations to regional tectonic history

5.2.1. Stage-wise evolution of U1489 sediments

Based on the provenance pattern discussed above, a stage-wise, tectonic-related variations in the siliciclastic supplies to Site U1489 can be identified, via the application of geochemical proxies for provenance, grain size, and weathering intensity (Fig. 6).

Using REE fractionation parameters as provenance proxies (i.e. Eu/Eu^* and La_N/Yb_N), during Stages II and III (before ~1.7 Ma), Site U1489 sediments are dominated by contributions from ultra-mafic/mafic rocks (Fig. 6a). During Stage I (after ~1.7 Ma), the data of Site U1489 approach to the regression line of the modern PNG-derived sediment (Wu et al., 2013), most likely due to a higher contribution of

metamorphic rock sources over time (Figs. 3a, b and 6a). Moreover, plots of UCC-normalized trace elements can shed light on the changes in source-rock types between the three stages as identified (Figs. 3 and 6c, d). The contribution from felsic rocks is minor and the sources of felsic contributions may remain compositionally constant over time, given the linear correlation of Th_C vs. Rb_C ($R^2 = 0.91$, Fig. 6d).

On the contrary, the contributions from mafic rocks should have substantially changed and dominated the variability of geochemical composition of Site U1489, for Stages II and III in particular (Figs. 3 and 6). Specifically, in the plot that represents elements of mafic-origin (i.e. Cr_C vs. Ni_C), there is a systematic trend in the data from sediments deposited during Stage II (Fig. 6c), indicating a single dominant source for that period (~3.5–1.7 Ma). By contrast, the similar range but rather scattered distribution for Stages I and III may indicate multiple types of mafic rock sources (Figs. 3d and 6c).

When looking closely, the features of Stage II are key to decipher the processes related to tectonic movements. The reduced values of both LREE and Eu/Eu^* may have resulted from an increased contribution from mafic rocks like ophiolite or from metamorphic rocks (Zirakparvar et al., 2013) (Fig. 3). Geochemically, the most marked difference between ophiolite and metamorphic rocks is that metamorphic rocks are more enriched in ΣREE (Zirakparvar et al., 2013; Kaczmarek et al., 2015). During Stage-II, the ΣREE decreases (Fig. 3a) and may reflect a relatively limited contribution of metamorphic rocks. However, this inference conflicts with the higher values of the trace-element ratios (i.e. Ni/Th and Cr/Rb) during Stage II-B which suggest an increased input of mafic materials (Fig. 3d). Instead, the changes in ΣREE can be best attributed to coarser grain size of siliciclastic particles, as evidently indicated by the increased ratios of Ti/Al and Zr/Rb (Figs. 6b and 2c).

At a first glance, the apparent contradiction of the geochemical signals in Stage II-A could be explained by somewhat increased influence of felsic materials inputted from the PNG landmasses. However, this case is largely discounted given the linear correlation between Th_C and Rb_C , indicating a relatively constant source of felsic rocks. Alternatively, these puzzling signals of Stage II-A can be reconciled by hypothesizing an increase in grain size of the siliciclastic particles (Figs. 6b and 2c), resulting from changes in the mode and strength of particle transport. This is supported by increased values of Ti/Al and Zr/Rb as grain-size proxies during Stage II-A (Fig. 2c). In fact, it has been shown that sediment grain size is mostly linked to tectonism, with higher values associated with major orogenic events, despite the possible modulations by factors like hydroclimate and vegetation cover (Wei and Algeo, 2020; and references therein).

Taken together, it appears to be the case that enhanced marginal mixing occurred during Stage II-A, leading to not only enhanced fluxes of felsic materials to Site U1489 (Fig. 6c), but also increased transport of coarser sediments over this interval (Figs. 6b and 2c). Besides, the coastal currents might be strengthened due to constriction of the seaway between PNG and the New Britain, causing coarser grain size in U1489 sediments (Figs. 1 and 6b).

The geochemical records of Site U1489 consistently indicate that more mafic materials have been transported to the WEP during Stage II-B (Fig. 3), most likely as a result of the exposure of some ophiolite terrane to the action of weathering by tectonics. Many tectonic reconstructions have shown that the late Pliocene around 4–3 Ma is a period when the Australian Plate moved northward and collided with and elevated the volcanic arcs in Timor-Banda Seas (Cane and Molnar, 2001; Hall, 2009; Karas et al., 2011; Baldwin et al., 2012; Christensen et al., 2017). In the PNG area, in association with the northward subduction of the Australian Plate, a series of tectonic consequences such as arc-continent collision, Bismarck Sea opening, and microplate rotation had occurred along the eastern PNG coast since the Late Pliocene (Holm et al., 2016). In other words, the changes seen here during Stage II-B (i.e. ~3.5–2.9 Ma) should be a direct result of tectonic collision along the eastern margin of PNG (Fig. 3).

To summarize, the three-stage evolution of Site U1489 sediments is

suggested by key REE fractionation parameters and trace-element ratios. In particular, frequent and large tectonic activities should have occurred in Stage II (~3.5–1.7 Ma), leading to enhanced contributions from mafic sources (i.e. Eu/Eu^* , La_N/Yb_N , and mafic/felsic elemental ratios of Ni/Th and Cr/Rb), and also coarser grain size due to more dynamic transport process and sedimentary environment (as seen from enhanced grain-size proxies of Ti/Al and Zr/Rb ratios, and the reduced ΣREE contents).

5.2.2. Refined picture of PNG tectonics

The geochemical results of the marine sediments recovered at IODP Site U1489 (Figs. 3 and 6) provide refined and detailed information and more precise timing of the tectonic evolution of eastern PNG arc-continent collision (Fig. 7, after Baldwin et al., 2012; Holm et al., 2016) since the Mid Pliocene to recent.

Stage III (before ~ 3.5 Ma). The Adelbert-Finisterre Terrane (AFT) and New Britain (NB) might have just started to collide with the mainland PNG (Fig. 7a). This was the time that the NB Trench reactivated subduction, as indicated by a source-rock type shift in the suture zone between the AFT and the mainland PNG between ~3.7–3.0 Ma (Johnson and Jaques, 1980; Abbott et al., 1994; Abbott, 1995; Holm and Richards, 2013). Magnetic evidence also suggests that the Finisterre-Huon Range initially uplifted around 3.5 Ma, and related rifting and extension occurred in association with the rapid opening of the Bismarck Sea (Taylor, 1979; Lee and Ruellan, 2006). Such a transition at ~3.5 Ma is clearly seen in the various provenance indicators in Fig. 3, and consistent with the relatively coarse particles as proxied by Ti/Al and Zr/Rb (Fig. 2c).

Stage II-B (~3.5–2.9 Ma). The arc-continent collision between AFT and mainland PNG might have intensified during this time (Abbott et al., 1994; Abbott, 1995) (Fig. 7b). The collision could have caused the increased supplies of ophiolite-related siliciclastic to Site U1489 as indicated by the largest values of Ni/Th and Cr/Rb (Fig. 3d), while the source areas and depositional environments may remain as the earlier Stage III due to the invariable Eu/Eu^* , La_N/Yb_N , and Ti/Al and Zr/Rb (Figs. 6a, b and 3c).

Stage II-A (~2.9–1.7 Ma). The AFT overthrust the eastern PNG continental margin (Fig. 7c), resulting in magmatism derived from underthrust continental crust (Holm et al., 2016; and references therein). This period is characterized by the typically mafic-sourced sediment composition, i.e., the most prominent positive Eu anomaly and LREE depletion (Fig. 3a–c). Moreover, the occurrence of coarsest sediment particles (as indicated by largest Ti/Al and Zr/Rb values; Fig. 2c) could reflect very dynamic transport processes, possibly with a marginal sediment recycling. Considering the close link between grain size and tectonism (Wei and Algeo, 2020; and references therein), Stage II-A appears to be the major orogenic phase of the eastern PNG mountain ranges.

Stage I (~1.7 Ma to the present). The collision between AFT and PNG gradually relaxed (Fig. 7d), forming the modern-like tectonic arrangement of the eastern PNG. Because of the continued docking of the Finisterre Terrane with the mainland PNG, the western NB Trench was accommodated to the Ramu-Markham Fault (Abbott et al., 1994; Abbott, 1995) (Fig. 7c, d). This accommodation may have provided a slab edge that stimulated subduction hinge retreat and resulted in the anticlockwise rotation of the South Bismarck Microplate and the NB Trench, leading to seafloor spreading in the Manus Basin (Govers and Wortel, 2005; Stegman et al., 2006). During this interval with stable tectonic backgrounds, a gradual increase in felsic influences might have occurred (Figs. 3 and 6a).

To sum up, the U1489 sediments reveal distinguishable evolutionary patterns in association with the tectonic history of the Eastern PNG margin. Besides the relatively stable Stages I (1.7–0 Ma) and III (4.0–3.5 Ma), major changes in the tectonic-controlled variations of U1489 sediment occurred during Stage II (3.5–1.7 Ma), which is most likely related to the collision of the Adelbert-Finisterre Terrane with the

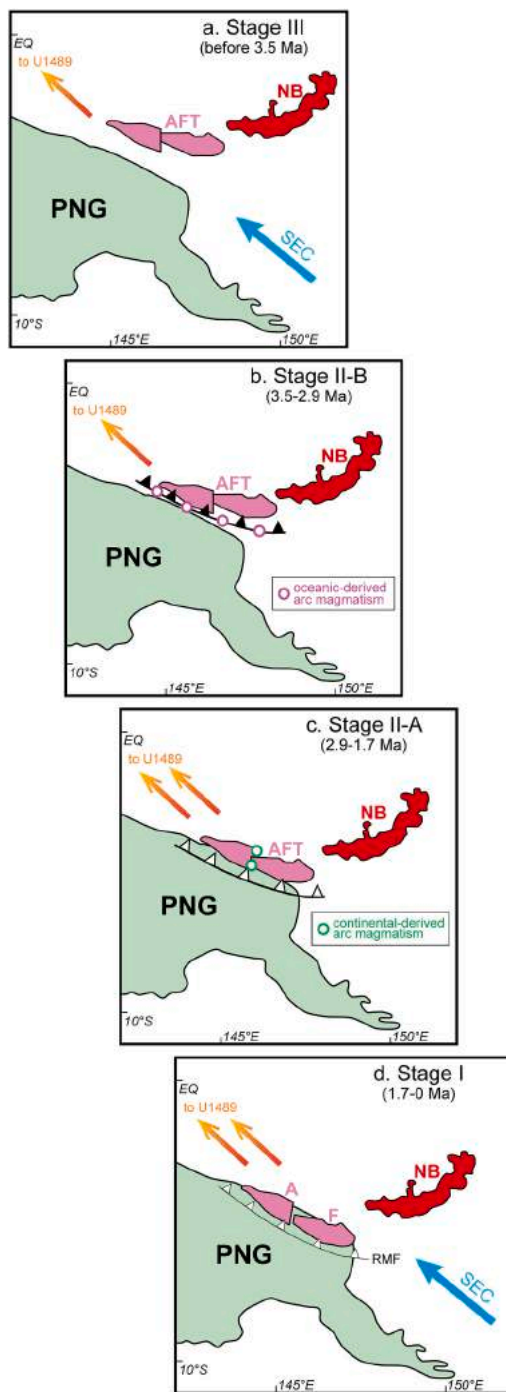


Fig. 7. Schematic view of tectonic sequences along the eastern PNG coast during the last 4 Ma. (a) Stage III (4–3.5 Ma): the Adelbert-Finisterre Terrane (AFT), coupling with New Britain (NB), was separated from PNG. (b) Stage II-B (3.5–2.9 Ma): the shelf of PNG started to subduct beneath AFT causing oceanic-crust derived arc magmatism, and the Adelbert, Finisterre and NB were decoupled from each other. (c) Stage II-A (2.9–1.7 Ma): AFT overthrust above the PNG continental margin, which underthrust into depth (~100 km) and resulted in continental-crust derived arc magmatism (at the boundary between Adelbert and Finisterre terranes); the decoupling and relative movement of the South and North Bismarck microplates widened the distance between AFT and NB. (d) Stage I (1.7–0 Ma): subduction of PNG underneath AFT weakened and slowed down, leaving a modern Ramu-Markham Fault zone (RMF). Plots and interpretations mainly adopted from Holm et al. (2016) with inputs from Baldwin et al. (2012).

mainland PNG (Fig. 7) (Abbott et al., 1994; 1995; Holm et al., 2016, and references therein).

At a local point of view, this event of Stage II re-organized the tectonic background of the eastern PNG area and re-shaped the source-rock characteristics of the sediment inputted to the WEP. In terms of the global climate change in association with the Northern Hemisphere Glaciation, the arc-continent collision of PNG region at 3.5–1.7 Ma coincides with the episodes of gradual cooling and climate-state reorganization (Ravelo et al., 2004), possibly supporting the hypothesis of tropical orogenesis on Earth's glacial cooling (MacDonald et al., 2019). The subsequent changes in the U1489 sediment composition took place under such a renewed background condition, and the hydroclimate variations should have played a dominant role in both changes in weathering regime and transport dynamic.

5.3. Climate-driven changes in weathering intensity

Interpretations of weathering intensity rely mainly on the major-element composition of Site U1489. However, the absolute CIA values are erratically low, i.e. between 40 and 70. This discrepancy could be explained by 1) the obscuration by the tectonic-dominated effect as discussed above, 2) a rapid and dynamic sediment delivery as supported by the enhanced ratios of Zr/Rb and Ti/Al as grain-size proxies (Milliman et al., 1999; Wei and Algeo, 2020) (Fig. 2c), or 3) the minor influence of carbonate diagenesis, organic matter remineralization, and clay mineral alteration as found in Site U1489 (Rosenthal et al., 2018). Further works are needed for the last matter.

In any case(s), given the consistent variations between the various proxies of chemical weathering (Fig. 2d–f), our results and interpretations contribute a better understanding of the evolution of weathering in PNG during the last 4 Ma. In short, the comparisons between Na/Al, Ca/Al, and K/Al ratios (Fig. 2a, b) and the various weathering indexes (Fig. 2d–f) show both consistencies and variances, suggesting that: (1) relative stable conditions during ~4.0–2.9 Ma, (2) a distinguishable decrease in weathering intensity during ~2.9–2.3 Ma, and (3) an overall increasing trend in weathering since ~2.3 Ma. Our results indicate that, for the major, rock-constituted elements (i.e. Na, Ca, K, Al), the PNG chemical weathering over the past 4 Ma is moderately intense and not sufficiently intense to leach K (see Section 5.1.1).

5.3.1. Increased weathering intensity since Mid-Pleistocene

Reconstructing the intensity of chemical weathering over the PNG region is of importance to the understanding of terrigenous input to the equatorial Pacific, which is meaningful for the regional climate and biogeochemistry (Wells et al., 1999; Dang et al., 2020a). With the inferred changes in source rock type and sediment transport process, the general trend indicated by the indexes of chemical weathering intensity (Fig. 8a) and elemental ratios (Fig. 8b) can be interpreted at a more detailed level.

Since regional tectonism dominates the geochemical variations in U1489 sediment before ~1.7 Ma, we may only propose an increasing trend of chemical weathering intensity after ~1.7 Ma (Stage I), when the tectonic activities in PNG and their effects on exposing different types of source-rocks (Fig. 8c) and reshaping regional transportation dynamics have remained relatively stable (Fig. 8d). It has been suggested that the zonal and meridional sea surface temperature (SST) gradients of the Pacific have increased over the Plio-Pleistocene (Wara et al., 2005; Jian et al., 2006; Zhang et al., 2014; Fedorov et al., 2015) (Fig. 8e, f), and as a result the atmospheric circulations has been enhanced and the rainfall over the western equatorial Pacific strengthened (Fedorov et al., 2015). It has also been proposed that the Pacific-Caribbean gateway appeared to be an incipient littoral-neritic leakage since ~2.4 Ma and finally closed around ~1.8 Ma (Keller et al., 1989), and such a seaway closure was suggested to be responsible for the cooling of the EEP and thus the strengthening of the W–E SST gradient (Steph et al., 2010; Zhang et al., 2012). However, the SST gradient change at ~1.7 Ma was shown to be a

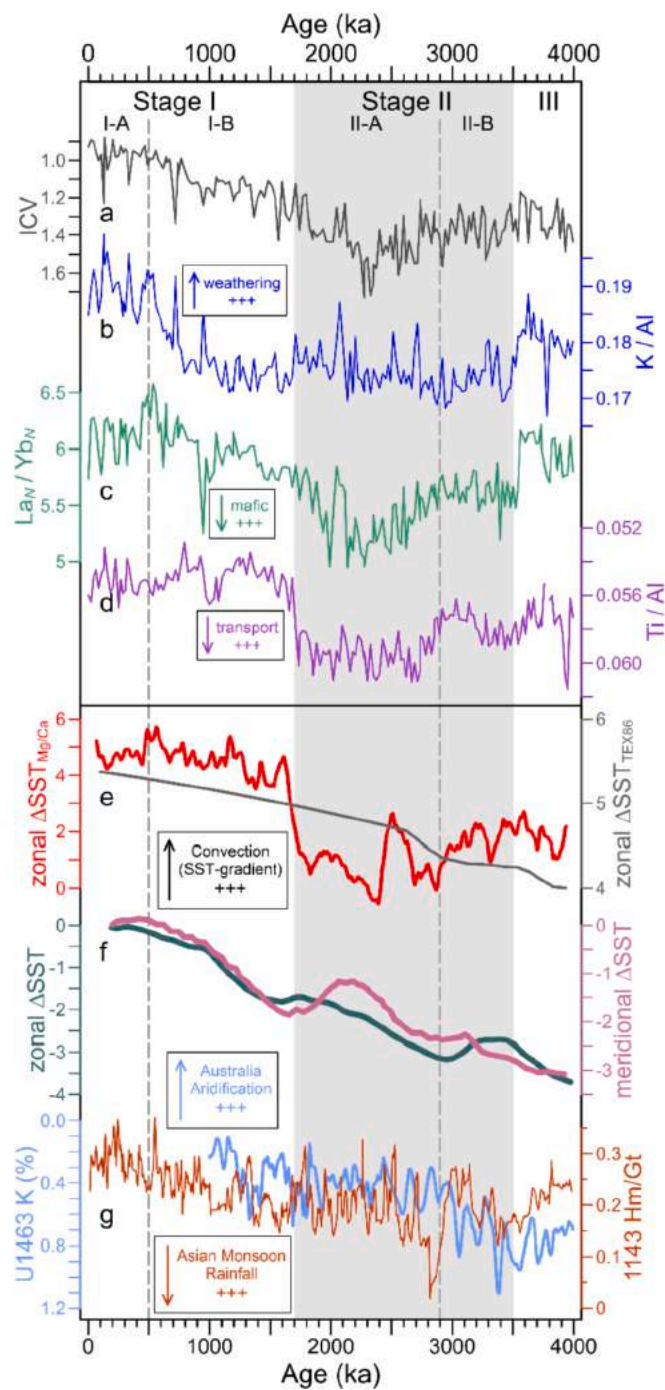


Fig. 8. Climate-driven weathering change over the PNG region in the last 4 Ma. (a, b) Indexes for weathering intensity, ICV (a, gray) and K/Al (b, blue). (c) Indicators of source rocks, La_N/Yb_N (c, green), and of grain size, Ti/Al (d, purple). (e, f) Sea surface temperature gradients (ΔSST) between the west and east tropical Pacific (zonal) of planktonic foraminifera Mg/Ca (e, red, Wara et al., 2005) and TEX86 (e, gray; Zhang et al., 2014), and the zonal (f, dark green) and meridional (f, dark purple, between the tropical and sub-tropical Pacific) ΔSST estimated by a multi-method compilation (Fedorov et al., 2015). (g) Proxies of the Asian Monsoon rainfall (brown, ratio between hematite and goethite contents of ODP Site 1143, southern South China Sea; Zhang et al., 2009) and the Australia aridification (light blue, potassium content of IODP Site U1463, northwestern off Australia; Christensen et al., 2017). Stage I through III and the sub-stages are denoted by vertical bars. (For interpretation of the references to colour in this figure legend, the reader is referred to the web version of this article.)

result of an abrupt warming in the WEP (Wara et al., 2005) with no obvious sign of cooling in the EEP (Liu et al., 2019). An SST warming in the WEP may have effectively enhanced the convective precipitation in the region, and consequently increased the chemical weathering intensity over PNG area.

An increasing weathering over PNG since ~ 1.7 Ma, as observed in U1489 sediment records (Fig. 8a, b), is consistent with the final establishment of the equatorial Pacific sea-air coupled system with an enlarged west-east SST gradient at this timepoint (Wara et al., 2005) (Fig. 8e), and with the continued increase in zonal and meridional SST gradients after ~ 1.7 Ma (Fedorov et al., 2015) (Fig. 8f). From the viewpoint of the meridional transect of Asia-WEP-Australia, the strengthening of chemical weathering intensity in WEP since ~ 1.7 Ma coincided with the long-term trends of aridification in Australia (Christensen et al., 2017) and Central Asia (Zhang et al., 2020), as well as a weakening in Asian summer monsoon (Zhang et al., 2009), possibly suggesting an anti-phased hydro-climatic evolution between the equatorial western Pacific and the mid-latitude continents at both hemispheres (Fig. 8g).

We thus conclude that, although the climate-driven changes should have increased the chemical weathering over PNG from the Pliocene to the latest Pleistocene, the tectonic-controlled evolution of source-rock compositions and sediment dynamics have substantially influenced the composition of the siliciclastic fraction at Site U1489 between ~ 4 and ~ 1.7 Ma. It is only during the last ~ 1.7 Ma, after tectonism in PNG became more quiescent, that the enhanced SST gradients and atmosphere circulation and the resultant strengthening of chemical weathering become prominent, as recorded by the elemental composition of Site U1489 sediments.

6. Conclusions

The long-term tectonic and climate evolutions over the realm where modern Papua New Guinea formed have caused ongoing changes in the terrigenous input to the western equatorial Pacific, with substantial oceanographic and biogeochemical consequences. By assessing the elemental geochemistry of the Plio-Pleistocene sediment sequence at IODP Site U1489, changes in the regional tectonic activity and climate condition over the last 4 Ma are studied.

Our results suggest that the siliciclastic fractions at Site U1489 are mainly originated from the PNG region, which consistently show a 3-stage pattern over the last 4 Ma. Major changes in the tectonic-related source-rock composition and associated sediment supply occurred during ~ 3.5 – 1.7 Ma, with significant increase in mafic materials like ophiolite, in association with the Adelbert-Finisterre Terrane collision with the mainland PNG. A persistent increase in the intensity of chemical weathering since ~ 1.7 Ma is reported for the PNG region for the first time, likely resulting from the enhanced sea surface temperature gradients and atmosphere circulation across the tropical Pacific.

Two key points in our sediment geochemical records of Site U1489, i. e., the enhanced mafic material contribution around ~ 2.9 Ma and the starting of increase in weathering intensity at ~ 1.7 Ma, coincide with the onset of Northern Hemisphere Glaciation and the abrupt strengthening of the W-E SST contrast across the equatorial Pacific, respectively. It is still unclear, however, if and how the weathering regime change of PNG is related to the glaciation and cooling during the Pliocene-Pleistocene transition, and the final establishment of the equatorial Pacific W-E air-sea coupled system in the Pleistocene. The exact role played by the late Neogene variations in tectonic collision and chemical weathering of the western tropical Pacific in global climate changes, as partly presented here, needs to be further investigated by quantitative proxy reconstructions and Earth-system numerical simulations.

Author statement

Hereby we confirm that this paper is new and has not been published

elsewhere and is not under consideration in whole or in part by another journal. All authors provided significant inputs to the manuscript and approve the final manuscript including the data as presented. As required, the individual contributions of each coauthor are specified as follows: HD and JZ designed the research. NP and HD performed the analyses. NP, HD and JW compiled and interpreted the data, and wrote the versions of the manuscript. IWA provided crucial suggestions to the data interpretation and manuscript.

Declaration of Competing Interest

The authors declare no competing interests.

Acknowledgement

This research used samples provided by the International Ocean Discovery Program. The authors thank all that participated in the IODP Expedition 363 and the Sampling Party. This work is supported financially by the National Key Research and Development Program of China (grant 2018YFE0202401), the Ministry of Natural Resources of China (grant GASI-GEOGE-04), and the National Natural Science Foundation of China (grants 91958208, 41830539, 42176053, 41630965, and 41606049). The authors thank Peijun Qiao for his assistance in the laboratory analyses. Constructive comments from the reviewer and editor are highly appreciated. A full dataset is available in the online Supplementary File and at Pangaea (www.pangaea.de).

References

- Abbott, L.D., 1995. Neogene tectonic reconstruction of the Adelbert-Finisterre-New Britain collision, northern Papua New Guinea. *J. SE Asian Earth Sci.* 11 (1), 33–51.
- Abbott, L.D., Silver, E.A., Galewsky, J., 1994. Structural evolution of a modern arc-continent collision in Papua New Guinea. *Tectonics* 13 (5), 1007–1034.
- Aiello, I.W., Bova, S.C., Holbourn, A.E., et al., 2019. Climate, sea level and tectonic controls on sediment discharge from the Sepik River, Papua New Guinea during the Mid- to Late Pleistocene. *Mar. Geol.* 415, 105954.
- Baldwin, S.L., Fitzgerald, P.G., Webb, L.E., 2012. Tectonics of the New Guinea Region. *Annu. Rev. Earth Planet. Sci.* 40 (1), 495–520.
- Bayon, G., Lambert, T., Vigier, N., De Deckker, P., et al., 2020. Rare earth element and neodymium isotope tracing of sedimentary rock weathering. *Chem. Geol.* 553, 119794.
- Borges, J., Huh, Y., 2007. Petrography and chemistry of the bed sediments of the Red River in China and Vietnam: provenance and chemical weathering. *Sediment. Geol.* 194 (3–4), 155–168.
- Borlace, S., Santoso, A., Cai, W., et al., 2014. Extreme swings of the South Pacific Convergence Zone and the different types of El Niño events. *Geophys. Res. Lett.* 41 (13), 4695–4703.
- Boyle, E.A., 1983. Chemical accumulation variations under the Peru current during the past 130,000 years. *J. Geophys. Res. Oceans* 88, 7667–7680.
- Burls, N.J., Fedorov, A.V., Sigman, D.M., et al., 2017. Active Pacific meridional overturning circulation (PMOC) during the warm Pliocene. *Sci. Adv.* 3 (9), e1700156.
- Butt, J., Lindstrom, E., 1994. Currents off the east coast of New Ireland, Papua New Guinea, and their relevance to regional undercurrents in the western equatorial Pacific Ocean. *J. Geophys. Res. Oceans* 99 (C6), 12503–12514.
- Cai, W.J., Lengaigne, M., Borlace, S., et al., 2012. More extreme swings of the South Pacific convergence zone due to greenhouse warming. *Nature* 488 (7411), 365–369.
- Cane, M.A., Molnar, P., 2001. Closing of the Indonesian seaway as a precursor to east African aridification around 3–4 million years ago. *Nature* 411 (6834), 157–162.
- Caves Rugenstein, J.K., Ibarra, D.E., von Blanckenburg, F., 2019. Neogene cooling driven by land surface reactivity rather than increased weathering fluxes. *Nature* 571, 99–102.
- Christensen, B.A., Renema, W., Henderiks, J., et al., 2017. Indonesian Throughflow drove Australian climate from humid Pliocene to arid Pleistocene. *Geophys. Res. Lett.* 44 (13), 6914–6925.
- Cloos, M., Sapiie, B., Ufford, A.Q.V., et al., 2005. Collisional delamination in New Guinea: the geotectonics of subducting slab breakoff. *Geol. Soc. Am.* 400 <https://doi.org/10.1130/2005.2400>.
- Condie, K.C., 1991. Another look at rare earth elements in shales. *Geochim. Cosmochim. Acta* 55 (9), 2527–2531.
- Cox, R., Lowe, D.R., Cullers, R.L., 1995. The influence of sediment recycling and basement composition on evolution of mudrock chemistry in the southwestern United States. *Geochim. Cosmochim. Acta* 59 (14), 2919–2940.
- Dang, H., Jian, Z., Kissel, C., Bassinot, F., 2015. Precessional changes in the western equatorial Pacific Hydroclimate: a 240 kyr marine record from the Halmahera Sea, East Indonesia. *Geochem. Geophys. Geosyst.* 16 (1), 148–164.
- Dang, H., Wu, J., Xiong, Z., et al., 2020a. Orbital and sea-level changes regulate the iron-associated sediment supplies from Papua New Guinea to the equatorial Pacific. *Quat. Sci. Rev.* 239, 106361.
- Dang, H., Peng, N., Ma, X., et al., 2020b. Possible linkage between the long-eccentricity marine carbon cycle and the deep-Pacific circulation: Western equatorial Pacific benthic foraminifera evidences of the last 4 Ma. *Mar. Micropaleontol.* 155, 101797.
- Davies, H.L., Jaques, A.L., 1984. Emplacement of ophiolite in Papua New Guinea. *Geol. Soc. London Spec. Publ.* 13 (1), 341–349.
- Dypvik, H., Harris, N.B., 2001. Geochemical facies analysis of fine-grained siliciclastics using Th/U, Zr/Rb and (Zr+Rb)/Sr ratios. *Chem. Geol.* 181, 131–146.
- Fedorov, A.V., Burls, N.J., Lawrence, K.T., et al., 2015. Tightly linked zonal and meridional sea surface temperature gradients over the past five million years. *Nat. Geosci.* 8 (12), 975–980.
- Fine, R.A., Lukas, R., Bingham, F.M., et al., 1994. The western equatorial Pacific: a water mass crossroads. *J. Geophys. Res. Oceans* 99 (C12), 25063–25080.
- Fralick, P.W., Kronberg, B.L., 1997. Geochemical discrimination of clastic sedimentary rock sources. *Sediment. Geol.* 113, 111–124.
- Gaillardet, J., Dupré, B., Louvat, P., Allègre, C.J., 1999. Global silicate weathering and CO₂ consumption rates deduced from the chemistry of large rivers. *Chem. Geol.* 159, 3–30.
- Garzanti, E., Vermeesch, P., Padoan, M., et al., 2014. Provenance of passive-margin sand (Southern Africa). *J. Geol.* 122 (1), 17–42.
- Gena, K., Mizuta, T., Ishiyama, D., Urabe, T., 2001. Acid-sulphate type alteration and mineralization in the Desmos Caldera, Manus back-arc basin, Papua New Guinea. *Resour. Geol.* 51, 31–44.
- Godfrey, J.S., Johnson, G.C., McPhaden, M.J., Reverdin, G., Wijffels, S., 2001. The tropical ocean circulation. In: Siedler, G., Church, J., Gould, J. (Eds.), *Ocean Circulation and Climate*. Academic Press, pp. 215–245.
- Gordon, A.L., 2005. Oceanography of the Indonesian seas and their throughflow. *Oceanography* 18 (4), 14–27.
- Govers, R., Wortel, M.J.R., 2005. Lithosphere tearing at STEP faults: Response to edges of subduction zones. *Earth Planet. Sci. Lett.* 236 (1–2), 505–523.
- Grenier, M., Cravatte, S., Blanke, B., et al., 2011. From the western boundary currents to the Pacific Equatorial Undercurrent: Modeled pathways and water mass evolutions. *J. Geophys. Res. Oceans* 118, 592–618.
- Hall, R., 2009. Southeast Asia's changing palaeogeography. *Blumea* 54 (1–2), 148–161.
- Hannigan, R.E., Sholkovitz, E.R., 2001. The development of middle rare earth element enrichments in freshwaters: weathering of phosphate minerals. *Chem. Geol.* 175, 495–508.
- Hartmann, J., Jansen, N., Dürr, H.H., et al., 2009. Global CO₂-consumption by chemical weathering: what is the contribution of highly active weathering regions? *Glob. Planet. Chang.* 69 (4), 185–194.
- Hartmann, J., Moosdorf, N., Lauerwald, R., et al., 2014. Global chemical weathering and associated P-release – the role of lithology, temperature and soil properties. *Chem. Geol.* 363, 145–163.
- Hay, W.W., Soeding, E., DeConto, R.M., Wold, C.N., 2002. The Late Cenozoic uplift-climate change paradox. *Int. J. Earth Sci. (Geol. Rundsch)* 91, 746–774.
- Haywood, A.M., Dowsett, H.J., Dolan, A.M., et al., 2016. The Pliocene Model Intercomparison Project (PlioMIP) Phase 2: scientific objectives and experimental design. *Clim. Past* 12, 663–675.
- Hill, K.C., Raza, A., 1999. Arc-continent collision in Papua Guinea: constraints from fission track thermochronology. *Tectonics* 18 (6), 950–966.
- Hollstein, M., Mohtadi, M., Rosenthal, Y., et al., 2018. Variations in Western Pacific Warm Pool surface and thermocline conditions over the past 110,000 years: Forcing mechanisms and implications for the glacial Walker circulation. *Quat. Sci. Rev.* 201, 429–445.
- Holm, R.J., Poke, B., 2018. Petrology and crustal inheritance of the Cloudy Bay Volcanics as derived from a fluvial conglomerate, Papuan Peninsula (Papua New Guinea): an example of geological inquiry in the absence of in situ outcrop. *Cogent Geosci.* 4 (1), 1450198.
- Holm, R.J., Richards, S.W., 2013. A re-evaluation of arc-continent collision and along-arc variation in the Bismarck Sea region, Papua New Guinea. *Aust. J. Earth Sci.* 60 (5), 605–619.
- Holm, R.J., Spandler, C., Richards, S.W., 2013. Melanesian arc far-field response to collision of the Ontong Java Plateau: geochronology and petrogenesis of the Simuku Igneous Complex, New Britain, Papua New Guinea. *Tectonophysics* 603, 189–212.
- Holm, R.J., Spandler, C., Richards, S.W., 2015. Continental collision, orogenesis and arc magmatism of the Miocene Maramuni arc, Papua New Guinea. *Gondwana Res.* 28 (3), 1117–1136.
- Holm, R.J., Rosenbaum, G., Richards, S.W., 2016. Post 8 Ma reconstruction of Papua New Guinea and Solomon Islands: Microplate tectonics in a convergent plate boundary setting. *Earth Sci. Rev.* 156, 66–81.
- Jian, Z., Yu, Y., Li, B., et al., 2006. Phased evolution of the south–north hydrographic gradient in the South China Sea since the middle Miocene. *Palaeogeogr. Palaeoclimatol. Palaeoecol.* 230 (3–4), 251–263.
- Johnson, R.W., Jaques, A.L., 1980. Continent–arc collision and reversal of arc polarity: new interpretations from a critical area. *Tectonophysics* 63 (1–4), 111–124.
- Kaczmarek, M.-A., Jonda, L., Davies, H.L., 2015. Evidence of melting, melt percolation and deformation in a supra-subduction zone (Marum ophiolite complex, Papua New Guinea). *Contrib. Mineral. Petrol.* 170 (2), 19.
- Karas, C., Nürnberg, D., Tiedemann, R., et al., 2011. Pliocene climate change of the Southwest Pacific and the impact of ocean gateways. *Earth Planet. Sci. Lett.* 301 (1–2), 117–124.
- Kashino, Y., Ueki, I., Kuroda, Y., et al., 2007. Ocean variability north of New Guinea derived from TRITON buoy data. *J. Oceanogr.* 63 (4), 545–559.

- Keller, G., et al., 1989. Late Neogene history of the Pacific-Caribbean gateway. *J. S. Am. Earth Sci.* 2 (1), 73–108.
- Kiladis, G.N., Von Storch, H., Loon, H., 1989. Origin of the South Pacific Convergence Zone. *J. Clim.* 2 (10), 1185–1195.
- Kroon, D., Shimmield, G., Shimmield, T., 2000. Century- to millennial-scale sedimentological geochemical records of the glacial-Holocene sediment variations from the Barra Fan (NE Atlantic). *J. Geol. Soc.* 157, 643–653.
- Lange, I.M., Reynolds, R.C., Lyons, J.B., 1966. K/Rb ratios in coexisting K-feldspars and biotites from some New England granites and metasediments. *Chem. Geol.* 1, 317–322.
- Lee, S.M., Ruellan, E., 2006. Tectonic and magmatic evolution of the Bismarck Sea, Papua New Guinea: review and new synthesis. *Am. Geophys. Union Geophys. Monogr. Ser.* 166, 263–286.
- Lee, Y.I., 2002. Provenance derived from the geochemistry of late Paleozoic–early Mesozoic mudrocks of the Pyeongan Supergroup. *Korea. Sediment. Geol.* 149 (4), 219–235.
- Li, C., Yang, S., 2012. Is Chemical Index of Alteration (CIA) a reliable proxy for chemical weathering in global drainage basins. *Am. J. Sci.* 310, 111–127.
- Li, G., Elderfield, H., 2011. Evolution of carbon cycle over the past 100 million years. *Geochim. Cosmochim. Acta* 103, 11–25.
- Li, X., Liu, Y., Tu, X., et al., 2002. Precise determination of chemical compositions in silicate rocks using ICP-AES and ICP-MS: a comparative study of sample digestion techniques of alkali fusion and acid dissolution. *Geochimica* 31, 289–294.
- Li, X., Wei, G., Shao, L., et al., 2003. Geochemical and Nd isotopic variations in sediments of the South China Sea: a response to Cenozoic tectonism in SE Asia. *Earth Planet. Sci. Lett.* 211, 207–220.
- Liu, J., Tian, J., Liu, Z., et al., 2019. Eastern equatorial Pacific cold tongue evolution since the late Miocene linked to extratropical climate. *Sci. Adv.* 5, eaau6060.
- Liu, L., Chen, J., Ji, J., Chen, Y., 2004. Comparison of paleoclimatic change from Zr/Rb ratios in Chinese loess with marine isotope records over the 2.6–1.2 Ma BP interval. *Geophys. Res. Lett.* 31, L15204.
- Liu, Z.F., Wang, H., Hantoro, W.S., et al., 2012. Climatic and tectonic controls on chemical weathering in tropical Southeast Asia (Malay Peninsula, Borneo, and Sumatra). *Chem. Geol.* 291, 1–12.
- Lu, H., Liu, R., Cheng, L., et al., 2020. Phased evolution and variation of the South Asian monsoon, and resulting weathering and surface erosion in the Himalaya–Karakoram Mountains, since late Pliocene time using data from Arabian Sea core. *Geol. Mag.* 157, 864–878.
- MacDonald, F.A., Swanson-Hysell, N.L., Park, Y., et al., 2019. Arc-continent collisions in the tropics set Earth's climate state. *Science* 364, 181–184.
- Matthewson, A.P., Shimmield, G.B., Kroon, D., et al., 1995. A 300 kyr high-resolution aridity record of the North African continent. *Paleoceanography* 10 (3), 677–692.
- McDonough, W.F., Sun, S.-S., 1995. The composition of the Earth. *Chem. Geol.* 120 (3–4), 223–253.
- McLennan, S.M., Hemming, S., McDaniel, D.K., Hanson, G.N., 1993. Geochemical approaches to sedimentation, provenance, and tectonics. *Geol. Soc. Am. Spec. Pap.* 284, 21–40.
- Melet, A., Gourdeau, L., Verron, J., 2010. Variability in Solomon Sea circulation derived from altimeter sea level data. *Ocean Dyn.* 60 (4), 883–900.
- Middelburg, J.J., van der Weijden, C.H., Woitiez, J.R., 1988. Chemical processes affecting the mobility of major, minor and trace elements during weathering of granitic rocks. *Chem. Geol.* 68, 253–273.
- Milliman, J.D., Farnsworth, K.L., Albertin, C.S., 1999. Flux and fate of fluvial sediments leaving large islands in the East Indies. *J. Sea Res.* 41, 97–107.
- Molnar, P., England, P., 1990. Late Cenozoic uplift of mountain ranges and global climate change: chicken or egg? *Nature* 346, 29–34.
- Nesbitt, H.W., Markovics, G., 1997. Weathering of granodioritic crust, long-term storage of elements in weathering profiles and petrogenesis of siliclastic sediments. *Geochim. Cosmochim. Acta* 61, 1653–1670.
- Nesbitt, H.W., Young, G.M., 1982. Early Proterozoic climates and plate motions inferred from major element chemistry of Lutites. *Nature* 299, 715–717.
- Oliva, P., Viers, J., Dupré, B., 2003. Chemical weathering in granitic environments. *Chem. Geol.* 202, 225–256.
- Pham, V.Q., Grenier, M., Cravatte, S., et al., 2019. Dissolved rare earth elements distribution in the Solomon Sea. *Chem. Geol.* 524, 11–36.
- Philander, S.G.H., 1983. El Niño Southern Oscillation phenomena. *Nature* 302, 295–301.
- Price, J.R., Velbel, M.A., 2003. Chemical weathering indices applied to weathering profiles developed on heterogeneous felsic metamorphic parent rocks. *Chem. Geol.* 202 (3–4), 397–416.
- Ravelo, A.C., Andreasen, D.H., Lyle, M., et al., 2004. Regional climate shifts caused by gradual global cooling in the Pliocene epoch. *Nature* 429, 263–267.
- Raymo, M.E., Ruddiman, W.F., 1992. Tectonic forcing of late Cenozoic climate. *Nature* 359, 117–122.
- Rosenthal, Y., Holbourn, A.E., Kulhanek, D.K., the Expedition 363 Scientists, 2018. Site U1489. In: Rosenthal, Y., Holbourn, A.E., Kulhanek, D.K., the Expedition 363 Scientists (Eds.), *Proceedings of the International Ocean Discovery Program Volume 363*. <https://doi.org/10.14379/iodp.proc.363.110.2018>.
- Rubin, J.N., Henry, C.D., Price, J.G., 1993. The mobility of zirconium and other “immobile” elements during hydrothermal alteration. *Chem. Geol.* 110, 29–47.
- Rudnick, R.L., Gao, S., 2003. Composition of the continental crust. In: Rudnick, R.L. (Ed.), *The Crust*. Elsevier-Peramgon, Oxford, pp. 1–64.
- Schneider, R.R., Price, B., Muller, P.J., Kroon, D., Alexander, I., 1997. Monsoon related variations in Zaire (Congo) sediment load and influence of fluvial silicate supply on marine productivity in the east equatorial Atlantic during the last 200,000 years. *Paleoceanography* 12, 463–481.
- Shao, L., Meng, A., Li, Q., et al., 2017. Detrital zircon ages and elemental characteristics of the Eocene sequence in IODP Hole U1435A: implications for rifting and environmental changes before the opening of the South China Sea. *Mar. Geol.* 394, 39–51.
- Slemons, L.O., Murray, J.W., Resing, J., et al., 2010. Western Pacific coastal sources of iron, manganese, and aluminum to the Equatorial Undercurrent. *Glob. Biogeochem. Cycles* 24 (3), GB3024.
- Smith, I.E.M., 2013. The chemical characterization and tectonic significance of ophiolite terrains in southeastern Papua New Guinea. *Tectonics* 32 (2), 159–170.
- Stegman, D.R., Freeman, J., Schellart, W.P., et al., 2006. Influence of trench width on subduction hinge retreat rates in 3-D models of slab rollback. *Geochem. Geophys. Geosyst.* 7 (3), 1–22.
- Steph, S., Tiedemann, R., Prange, M., et al., 2010. Early Pliocene increase in thermohaline overturning: a precondition for the development of the modern equatorial Pacific cold tongue. *Paleoceanography* 25, PA2202.
- Sun, Y., Wu, F., Clemens, S.C., Oppo, D.W., 2008. Processes controlling the geochemical composition of the South China Sea sediments during the last climatic cycle. *Chem. Geol.* 257, 240–246.
- Taboada, T., Cortizas, A.M., Garcia, C., Garcia-Rodeja, E., 2006. Particle-size fractionation of titanium and zirconium during weathering and pedogenesis of granitic rocks in NW Spain. *Geoderma* 131, 218–236.
- Tachikawa, K., Cartapanis, Q., Vidal, L., et al., 2011. The precession phase of hydrological variability in the Western Pacific Warm Pool during the past 400 ka. *Quat. Sci. Rev.* 30, 3716–3727.
- Taylor, B., 1979. Bismarck Sea: evolution of a back-arc basin. *Geology* 7 (4), 171–174.
- Tierney, J.E., Haywood, A.M., Feng, R., et al., 2019. Pliocene warmth consistent with greenhouse gas forcing. *Geophys. Res. Lett.* 46, 9136–9144.
- Trenberth, K.E., Stepaniak, D.P., Caron, J.M., 2000. The Global Monsoon as seen through the divergent atmospheric circulation. *J. Clim.* 13, 3969–3993.
- Tsuchiya, M., Lukas, R., Fine, R.A., et al., 1989. Source waters of the Pacific equatorial undercurrent. *Prog. Oceanogr.* 23 (2), 101–147.
- Vincent, D.G., 1994. The South Pacific convergence zone (SPCZ): a review. *Mon. Weather Rev.* 122 (9), 1949–1970.
- Vital, H., Statterger, K., 2000. Major and trace elements of stream sediments from the lowermost Amazon River. *Chem. Geol.* 168, 151–168.
- Walsh, J., Nittrouer, C., 2003. Contrasting styles of off-shelf sediment accumulation in New Guinea. *Mar. Geol.* 196 (3–4), 105–125.
- Wang, B., Wu, R., Li, T., 2003. Atmosphere–warm Ocean interaction and its impacts on Asian–Australian monsoon variation. *J. Clim.* 16, 1195–1211.
- Wara, M.W., Ravelo, A.C., Delaney, M.L., 2005. Permanent El Niño-like conditions during the Pliocene warm period. *Science* 309 (5735), 758–761.
- Webster, P.J., Magana, V.O., Palmer, T.N., et al., 1998. Monsoons: processes, predictability, and the prospects for prediction. *J. Geophys. Res. Oceans* 103 (C7), 14451–14510.
- Wei, G., Liu, Y., Li, X., et al., 2003. High-resolution elemental records from the South China Sea and their paleoproductivity implications. *Paleoceanography* 18 (2), 1054.
- Wei, W., Algeo, T.J., 2020. Secular variation in the elemental composition of marine shales since 840 Ma: tectonic and seawater influences. *Geochim. Cosmochim. Acta* 287, 367–390.
- Wells, M.L., Vallis, G.K., Silver, E.A., 1999. Tectonic processes in Papua New Guinea and past productivity in the eastern equatorial Pacific Ocean. *Nature* 398 (6728), 601–604.
- West, A.J., Galy, A., Bickle, M., 2005. Tectonic and climatic controls on silicate weathering. *Earth Planet. Sci. Lett.* 235, 211–228.
- Woodhead, J., Hergt, J., Sandiford, M., et al., 2010. The big crunch: Physical and chemical expressions of arc/continent collision in the Western Bismarck arc. *J. Volcanol. Geotherm. Res.* 190 (1–2), 11–24.
- Wu, J., Liu, Z., Zhou, C., 2012. Late quaternary glacial cycle and precessional period of clay mineral assemblages in the western Pacific warm pool. *Chin. Sci. Bull.* 57, 3748–3760.
- Wu, J., Liu, Z., Zhou, C., 2013. Provenance and supply of Fe-enriched terrigenous sediments in the western equatorial Pacific and their relation to precipitation variations during the late Quaternary. *Glob. Planet. Chang.* 108, 56–71.
- Wu, J., Filippidi, A., Davies, G.R., de Lange, G.J., 2018. Riverine supply to the eastern Mediterranean during last interglacial sapropel S5 formation: a basin-wide perspective. *Chem. Geol.* 485, 74–89.
- Yang, S., Jung, H.S., Choi, M.S., Li, C., 2002. The rare earth element compositions of the Changjiang (Yangtze) and Huanghe (Yellow) river sediments. *Earth Planet. Sci. Lett.* 201 (2), 407–419.
- Yang, S., Yim, W.W., Huang, G., et al., 2008. Geochemical composition of inner shelf Quaternary sediments in the northern South China Sea with implications for provenance discrimination and paleoenvironmental reconstruction. *Global Planet. Change* 60 (3), 207–221.
- Yim, B.Y., Yeh, S.W., Sohn, B.J., 2016. ENSO-related precipitation and its statistical relationship with the walker circulation trend in CMIP5 AMIP models. *Atmosphere* 7, 19.
- Yu, Z., Wan, S., Colin, C., et al., 2016. Co-evolution of monsoonal precipitation in East Asia and the tropical Pacific ENSO system since 2.36Ma: New insights from high-resolution clay mineral records in the West Philippine Sea. *Earth Planet. Sci. Lett.* 446, 45–55.
- Yu, Z., Wan, S., Colin, C., et al., 2018. ENSO-Like modulated tropical Pacific climate changes since 2.36 Myr and its implication for the Middle Pleistocene Transition. *Geochem. Geophys. Geosyst.* 19, 415–426.
- Zhang, Q., Liu, Q., Roberts, A.P., et al., 2020. Mechanism for enhanced eolian dust flux recorded in North Pacific Ocean sediments since 4.0 Ma: Aridity or humidity at dust source areas in the Asian interior? *Geology* 48, 77–81.

Zhang, X., Prange, M., Steph, S., et al., 2012. Changes in equatorial Pacific thermocline depth in response to Panamanian seaway closure: Insights from a multi-model study. *Earth Planet. Sci. Lett.* 317–318, 76–84.

Zhang, Y.G., Ji, J., Balsam, W., Liu, L., Chen, J., 2009. Mid-Pliocene Asian monsoon intensification and the onset of Northern Hemisphere glaciation. *Geology* 37 (7), 599–602.

Zhang, Y.G., Pagani, M., Liu, Z., et al., 2014. A 12-million-year temperature history of the tropical Pacific Ocean. *Science* 344 (6179), 84–87.

Zirakparvar, N.A., Baldwin, S.L., Vervoort, J.D., 2013. The origin and geochemical evolution of the Woodlark Rift of Papua New Guinea. *Gondwana Res.* 23 (3), 931–943.